



Repositioning small molecule drugs as allosteric inhibitors of the BFT-3 toxin from enterotoxigenic *Bacteroides fragilis*

Ana Jimenez-Alesanco^{1,2} | Ulrich Eckhard³ | Marta Asencio del Rio^{1,4} |
 Sonia Vega¹ | Tibisay Guevara³ | Adrian Velazquez-Campoy^{1,2,4,5}  |
 Francesc Xavier Gomis-Rüth³  | Olga Abian^{1,2,4,5}

¹Institute for Biocomputation and Physics of Complex Systems (BIFI), Joint Unit GBsC-CSIC-BIFI, Universidad de Zaragoza, Zaragoza, Spain

²Departamento de Bioquímica y Biología Molecular y Celular, Universidad de Zaragoza, Zaragoza, Spain

³Proteolysis Laboratory, Department of Structural Biology, Molecular Biology Institute of Barcelona (IBMB), Higher Scientific Research Council (CSIC), Barcelona, Catalonia, Spain

⁴Instituto de Investigación Sanitaria de Aragón (IIS Aragón), Zaragoza, Spain

⁵Centro de Investigación Biomédica en Red en el Área Temática de Enfermedades Hepáticas Digestivas (CIBERehd), Madrid, Spain

Correspondence

Adrian Velazquez-Campoy and Olga Abian, Department of Biochemistry and Molecular and Cellular Biology, Institute of Biocomputation and Physics of Complex Systems, University of Zaragoza, 50018 Zaragoza, Spain.
 Email: adrianvc@unizar.es and oabifra@unizar.es

Francesc Xavier Gomis-Rüth, Proteolysis Laboratory, Department of Structural Biology, Molecular Biology Institute of Barcelona (IBMB), Higher Scientific Research Council (CSIC), 08028 Barcelona, Catalonia, Spain.
 Email: xgrcri@ibmb.csic.es

Funding information

Centro de Investigación Biomédica en Red de Enfermedades Hepáticas y Digestivas; Fundació la Marató de TV3, Grant/Award Number: 201815; Gobierno de Aragón, Grant/Award Numbers: E25_20R,

Abstract

Bacteroides fragilis is an abundant commensal component of the healthy human colon. However, under dysbiotic conditions, enterotoxigenic *B. fragilis* (ETBF) may arise and elicit diarrhea, anaerobic bacteremia, inflammatory bowel disease, and colorectal cancer. Most worrisome, ETBF is resistant to many disparate antibiotics. ETBF's only recognized specific virulence factor is a zinc-dependent metalloprotease (MP) called *B. fragilis* toxin (BFT) or fragilysin, which damages the intestinal mucosa and triggers disease-related signaling mechanisms. Thus, therapeutic targeting of BFT is expected to limit ETBF pathogenicity and improve the prognosis for patients. We focused on one of the naturally occurring BFT isoforms, BFT-3, and managed to repurpose several approved drugs as BFT-3 inhibitors through a combination of biophysical, biochemical, structural, and cellular techniques. In contrast to canonical MP inhibitors, which target the active site of mature enzymes, these effectors bind to a distal allosteric site in the proBFT-3 zymogen structure, which stabilizes a partially unstructured, zinc-free enzyme conformation by shifting a zinc-dependent disorder-to-order equilibrium. This yields proBTF-3 incompetent

Abbreviations: ANS, 1-anilino-8-naphthalene sulfonic acid; BFT, *Bacteroides fragilis* toxin or fragilysin; CD, catalytic domain; CD, circular dichroism; CDP, conditionally disordered protein; DMEM, Dulbecco's modified Eagle medium; DMSO, dimethyl sulfoxide; DSF, differential scanning fluorimetry; EDTA, Ethylenediaminetetraacetic acid; ETBF, enterotoxigenic *Bacteroides fragilis*; HCV, hepatitis C virus; ITC, isothermal titration calorimetry; MP, metalloprotease; NEAA, non-essential amino acid; NS3, nonstructural protein 3; NTBF, non-enterotoxigenic *Bacteroides fragilis*; PBS, phosphate-buffered saline; PD, prodomain; RIPA, radioimmunoprecipitation assay buffer; TSA, thermal shift assay; UV, ultraviolet.

Ana Jimenez-Alesanco and Ulrich Eckhard contributed equally.

This is an open access article under the terms of the [Creative Commons Attribution-NonCommercial-NoDerivs](https://creativecommons.org/licenses/by-nc-nd/4.0/) License, which permits use and distribution in any medium, provided the original work is properly cited, the use is non-commercial and no modifications or adaptations are made.

© 2022 The Authors. *Protein Science* published by Wiley Periodicals LLC on behalf of The Protein Society.

E45_20R; Instituto de Salud Carlos III, Grant/Award Number: CPII13/00017; Ministerio de Ciencia e Innovación, Grant/Award Number: PID2019-107725RG-I00; Secretaría de Estado de Investigación, Desarrollo e Innovación, Grant/Award Number: BFU2016-78232-P; Catalan Agency, Grant/Award Number: 2017SGR3; Diputación General de Aragón Predoctoral Research Contract 2019; European Union, Grant/Award Numbers: PI21/00394, PI18/00349

Review Editor: Aitziber Cortajarena

for autoactivation, thus ablating hydrolytic activity of the mature toxin. Additionally, a similar destabilizing effect is observed for the activated protease according to biophysical and biochemical data. Our strategy paves a novel way for the development of highly specific inhibitors of ETBF-mediated enteropathogenic conditions.

KEYWORDS

allosteric inhibitors, *Bacteroides fragilis*, drug repurposing, fragilysin, molecular experimental screening, zinc-dependent metalloproteases

1 | INTRODUCTION

The human colon hosts the largest population of bacteria of the human body. Notably, approximately 25% of its species belong to the genus *Bacteroides*, which are anaerobic, bile-resistant, and non-spore-forming Gram-negative rods.¹ Although *Bacteroides* are normally commensals, several species can cause severe infections in the intra-abdominal space, for example after rupture of the gastrointestinal tract or intestinal surgery.^{2,3} After infiltration of the normally sterile peritoneal cavity by gut bacteria, first aerobes such as *Escherichia coli* dominate the infection. However, once sufficient oxygen has been depleted, *Bacteroides* typically dictate the chronic stage. Crucially, untreated *Bacteroides fragilis* infections lead to mortality rates of ~60%.^{4,5}

Among *Bacteroides*, *B. fragilis* accounts for only 0.5% of the human colon microbiome, but it is the most frequent anaerobic isolate in clinical specimens,¹ among which enterotoxigenic *B. fragilis* (ETBF) strains are considered the most virulent.^{2,6} Remarkably, the only recognized virulence factor specific to ETBF when compared to its nontoxic counterparts (NTBF) is a unique 20-kDa zinc-dependent metalloprotease (MP) dubbed fragilysin or *B. fragilis* enterotoxin (BFT),^{7,8} which is not found in any other organism, and is only very distantly related to ADAM/adamalysin MPs.⁹ The enzyme is encoded as three isoforms of >90% sequence identity (BFT-1, -2, and -3)^{7,8,10} by a 6-kb pathogenicity island (*BfPAI*) unique to ETBF,^{8,11} which is flanked by conjugative transposons. Thus, it may be transmitted to NTBF strains by lateral gene transfer.¹²

BFT can degrade the *zonula adherens* tight junctions of the intestinal epithelium by cleaving E-cadherin,^{7,13,14} thereby causing (a) delocalization of other tight-junction proteins, (b) loss of cell adhesion, (c) rearrangement of actin cytoskeleton, (d) nuclear translocation of β -catenin, (e) secretion of inflammatory signaling molecules, and (f)

loss of fluids, which collectively cause diarrhea and other related pathologies.³ As a consequence, patients with ETBF exhibit an increased risk for inflammatory bowel disease and colorectal cancer.^{3,15} Indeed, BFT expression is associated with early-stage carcinogenic lesions,¹⁶ and it has been shown that BFT activates both the NF- κ B and β -catenin/Tcf signaling pathways, thereby upregulating the c-Myc oncogene and the proinflammatory cytokine IL-8, which are both associated with colorectal cancer.^{17–20} To tackle *Bacteroides* infections, β -lactams co-administered with β -lactamase inhibitors, carbapenems, clindamycin, and metronidazole are frequently prescribed, the latter two often in combination with fluoroquinolones.²¹ However, several *B. fragilis* strains are intrinsically resistant to several classes of structurally unrelated antibiotics.^{22–25} Thus, specific inhibition of BFT represents an attractive novel route to combat ETBF-mediated pathogenicity in inflammatory bowel disease and colorectal cancer without disturbing the commensal microbiota.

Here, we describe a comprehensive drug discovery approach to target (pro)BFT-3. Starting from a collection of 1,120 drugs approved by the United States Food and Drug Administration, we identified compounds capable of specifically binding to the catalytic domain (CD) of (pro)BFT-3 by a molecular experimental screening based on differential scanning fluorimetry (DSF), which assessed ligand-induced stabilization of the protein against thermal denaturation through fluorescence emission spectroscopy. For this, we applied a strategy specially designed for zinc-dependent proteins, which assumes the existence of a physiologically relevant conformational state in the absence of the zinc cofactor. This strategy has proven successful previously for the identification of allosteric inhibitors of the hepatitis C virus (HCV) NS3 protease.²⁶ Hit compounds were subsequently assessed for target engagement, cytotoxicity, and biological efficacy using both in vitro assays and cell-based E-cadherin processing assays. Furthermore, we determined five crystal structures of

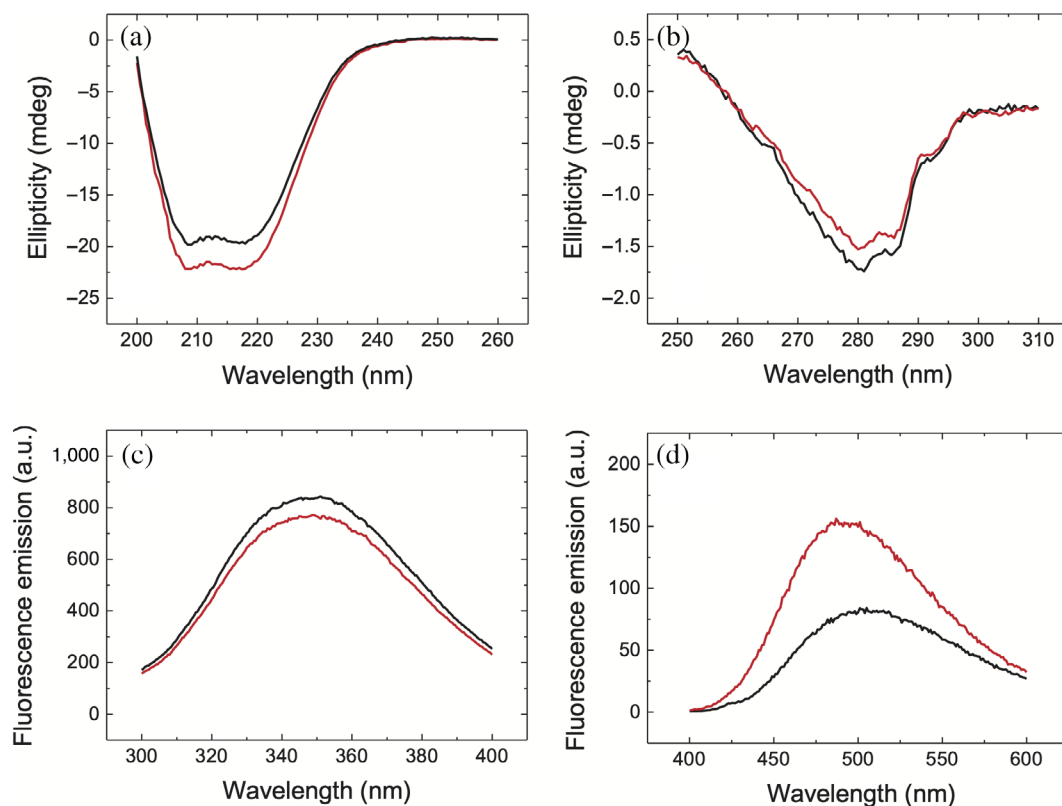


FIGURE 1 Spectroscopic characterization of proBFT-3. Spectra were recorded in the presence (black) and absence (red) of zinc. (a) Far-UV CD spectra and (b) near-UV CD spectra. Raw ellipticity data obtained with 10 μ M protein are shown. (c) Fluorescence spectra (excitation wavelength, 280 nm). Data obtained with 2 μ M protein. (d) 1-anilino-8-naphthalene sulfonic acid (ANS) fluorescence spectra (excitation wavelength, 370 nm) with proBFT-3. Data obtained with 2 μ M protein and 100 μ M ANS are shown

proBFT-3, unbound and complex with three of these inhibitors, which uncovered a hitherto unknown distal exosite on the surface opposed to the active-site cleft that crucially impacts the active-site geometry and, thus, activation of proBFT-3 through a unique mechanism of allosteric inhibition. Additionally, as the exosite is located within the CD, a similar destabilizing and inhibitory effect was observed for activated BFT-3. Therefore, because the inhibitors do not bind into the active site, they allosterically affect both proBFT-3 and BFT-3. Importantly, the identified compounds can be either considered straightforward for drug repurposing in combination therapies, or for lead optimization to obtain even more potent compounds against ETBF.

2 | RESULTS

2.1 | proBFT-3 is a zinc-dependent conditionally disordered protein

We employed several biophysical techniques, including circular dichroism (CD), DSF, and both intrinsic and

extrinsic fluorescence probes to assess the zinc-dependence of proBFT-3. As expected from the published structure, which evinces an α -helical content of $\sim 25\%$,⁹ the far-UV CD spectrum revealed a marked negative band at around 220 nm (Figure 1a). Unexpectedly, this peak increased by $\sim 11\%$ upon ethylenediaminetetraacetic acid (EDTA)-mediated zinc removal while no other major changes were observed. Importantly, the near-UV CD spectrum was non-zero (Figure 1b), which is indicative of a folded structure, and showed small changes upon zinc removal. The intrinsic fluorescence signal at 350 nm was reduced by $\sim 10\%$ (Figure 1c), pinpointing conformational changes in the local microenvironment of at least one of the four tryptophan residues in the CD of proBFT-3. Next, we investigated the impact of zinc dissociation using the extrinsic fluorescent probe 1-anilino-8-naphthalene sulfonic acid (ANS) as a hydrophobic reporter (Figure 1d). In the zinc-bound form, a fluorescence spectrum with a maximum intensity at around 505 nm was recorded, which is lower than the typical value of 535 nm for free ANS in an aqueous solvent and rather conforms to protein-bound ANS.²⁷ Upon zinc removal, this blue-shift was enhanced to ~ 490 nm, and

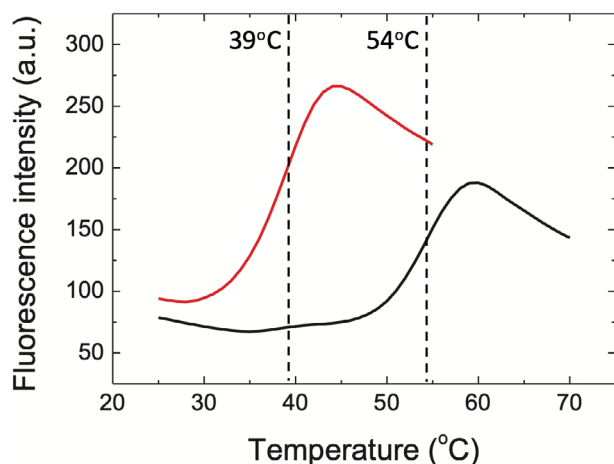


FIGURE 2 Thermal stability of proBFT-3 assessed by differential scanning fluorimetry (DSF). Thermal unfolding of proBFT-3 was monitored by DSF in the presence (black) and absence (red) of zinc. Thermograms were obtained with 2 μ M protein and 5X SYPRO Orange. For zinc-free proBFT-3, EDTA was added. For zinc-bound proBFT-3, no exogenous zinc was added; therefore, zinc concentration was that corresponding to the endogenous zinc accompanying proBFT-3 along the purification. Thus, a minor population of zinc-free enzyme could be observed (small positive slope at 39°C in the black line). The zinc bound to proBFT-3 increased the T_m from 39 to 54°C ($\Delta T_m = 15^\circ\text{C}$)

the recorded fluorescence intensity nearly doubled, indicating a potential conformational change accompanying the cofactor dissociation together with an increase in solvent-exposed protein surface.

In addition, thermal denaturation monitored by DSF showed that zinc-bound proBFT-3 unfolds in a single highly-cooperative transition, which indicates a high folding barrier and a sharp unfolding equilibrium (Figure 2). The unfolding temperature T_m of 54°C was in good agreement with the previously reported value of 56°C⁹ and an unfolding enthalpy $\Delta H(T_m)$ of 101 kcal/mol was estimated. Remarkably, zinc depletion caused a substantial reduction of the protein stability as revealed by the unfolding temperature and the associated unfolding enthalpy (39°C and 74 kcal/mol).

2.2 | Identification of ligands targeting the zinc-free partially disordered proBFT-3 state

In a previous study, we identified several small molecules as allosteric inhibitors of HCV NS3 protease, which stabilized the zinc-free—and thus an inactive and partially unfolded protein conformation—through a novel mechanism.²⁶ Leveraging the overall similarity of BFT-3 and NS3 as zinc-dependent MPs, we implemented a similar

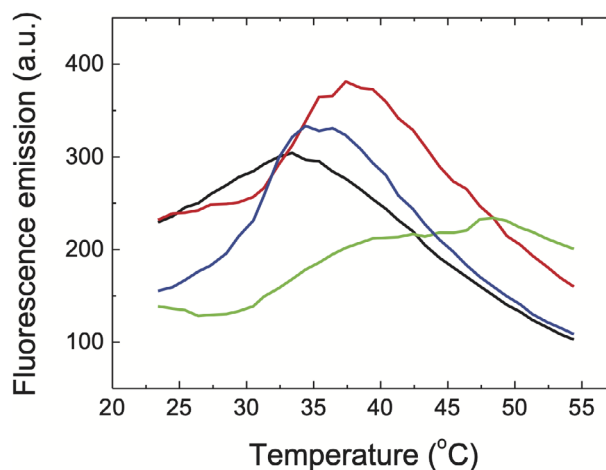


FIGURE 3 Experimental screening of compounds by thermal shift assay. Potential ligands of zinc-free proBFT-3 were identified as those molecules increasing the protein unfolding temperature by at least 3°C. Raw fluorescence intensity data as a function of temperature is shown for compound-free protein and for protein in the presence of selected compounds. Color coding: no compound (black), C-4 (red), C-9 (blue), and C-10 (green)

experimental strategy for targeting proBFT-3 by screening an FDA-approved chemical library to identify compounds capable to (a) induce stabilization of proBFT-3 against thermal unfolding, and (b) trap proBFT-3 in its zinc-free and thus inactive conformation.

Thermal unfolding in the presence and absence of small molecule compounds was monitored by following the emission signal of the extrinsic fluorescent probe SYPRO Orange, and using the Prestwick Chemical Library, a collection of 1,120 FDA-approved drugs with known therapeutic indication, good bioavailability, and safety in humans, and covering a large chemical and pharmacological space, as the screening set. Initial hits were identified as those compounds substantially increasing the unfolding temperature of zinc-free proBFT-3 at least by 3°C (Figure 3), and selected for further testing (Table 1). The known therapeutic indication for each of the compounds is reported in Table S3.

2.3 | Target engagement of selected compounds

As ligand-induced stabilization of proBFT-3 represents indirect evidence for interaction and there is no direct correlation between protein stabilization extent (i.e., ΔT_m) and ligand affinity (K_a), we determined the dissociation constants for selected compounds by isothermal titration calorimetry (ITC) to assess target engagement. Calorimetric assays were performed for all

TABLE 1 Dissociation constants of the proBFT-3-compound complexes obtained by ITC at 25°C and pH 7.4

| Compound | Zn (\pm) | K_a (M^{-1}) | K_d (μM) | ΔH (kcal/Mol) | n |
|----------|--------------|-------------------------------------------------------------|-------------------|-----------------------|------------------|
| C-4 | -Zn | 1.3×10^5 (1.2×10^5 - 1.4×10^5) | 7.8 (7.3-8.2) | -5.7 (-5.9 to -5.5) | 0.76 (0.72-0.74) |
| | +Zn | 5.0×10^4 (4.4×10^4 - 5.6×10^4) | 20 (18-23) | -9.1 (-10.5 to -8.1) | 0.73 (0.71-0.80) |
| C-9 | -Zn | 1.2×10^5 (1.1×10^5 - 1.2×10^5) | 8.5 (8.0-8.9) | -6.8 (-7.1 to -6.6) | 0.67 (0.66-0.68) |
| | +Zn | 6.9×10^4 (6.3×10^4 - 7.6×10^4) | 14 (13-16) | -10.2 (-11.2 to -9.4) | 0.66 (0.62-0.69) |
| C-10 | -Zn | 1.2×10^5 (1.1×10^5 - 1.2×10^5) | 8.7 (8.2-9.2) | -3.6 (-3.7 to -3.5) | 0.83 (0.82-0.85) |
| | +Zn | 4.6×10^4 (3.7×10^4 - 5.6×10^4) | 22 (18-27) | -7.5 (-8.8 to -6.1) | 0.67 (0.55-0.75) |

Note: The uncertainty in the estimation of the binding parameters is reported as the confidence interval at a statistical significance of 68%, shown in parenthesis below each parameter.

Abbreviations: ITC, isothermal titration calorimetry; K_a , association constant; K_d , dissociation constant; n , binding stoichiometry (or percentage of binding-competent protein); ΔH , binding enthalpy.

compounds with proBFT-3 in the presence/absence of the active-site zinc (Figure 4). Compounds C-4, C-9, and C-10 exhibited dissociation constants in the low micromolar range, and importantly, the presence of zinc caused an approximately two to threefold reduction in binding affinity, which was most pronounced for compounds C-4 and C-10. Interestingly, the binding enthalpies were more favorable for the zinc-bound proBFT-3, suggesting that the entropic contribution of the binding is either less favorable or more unfavorable in the zinc-free protein. Additional experiments done with trypsin-activated BFT-3 in the presence/absence of the active-site zinc provided similar binding affinities and similar influence of the zinc cofactor (see Table S4). Noticeably, the binding enthalpies were more favorable (i.e., more negative) than those for proBFT-3, and, therefore, the binding entropies were less favorable or more unfavorable than those determined for proBFT-3.

2.4 | Selected compounds inhibit BFT-3 in vitro

To evaluate the potential inhibitory effect of the selected compounds on the BFT-3 proteolytic activity, the commercial EnzChek Protease Assay kit was employed. Presence of proteolytic activity leads to the processing of the quenched BODIPY FL casein substrate, causing an increase in fluorescence intensity that is directly proportional to the enzymatic activity (Figure 5). Activity was determined for trypsin-activated BFT-3, for proBFT-3, and for trypsin alone as a positive control to assess its potential contribution to the overall signal. As expected, an increase in fluorescence over time could be observed for BFT-3, but not proBFT-3 (see Figure S1), and in presence of the compounds, a dose-dependent inhibition was detected (Figure 5).

2.5 | Cytotoxicity of the selected compounds

Cytotoxicity was tested on HT-29 and HeLa cells at the maximum compound concentration used in any of the assays, namely 400 μM (Figure 6). Importantly, compounds showed little or no cytotoxic effect, indicating that the cytotoxic concentration, CC_{50} , is significantly larger and that there is a potential therapeutic window for inhibition.

2.6 | Selected compounds inhibit E-cadherin processing

Western blot assays were performed to assess whether the selected compounds were able to hamper E-cadherin hydrolysis in HT-29 cells. Intact E-cadherin was observed as a single band at ~ 120 kDa, whereas processed E-cadherin could be observed as a band at ~ 80 kDa, which corresponds to the E-cadherin ectodomain.¹⁴ It was established from cytotoxic assays that compounds showed little toxicity and concentrations up to 200 μM are safe in cell assays. Compounds C-4, C-9, and C-10 reduced the levels of the E-cadherin processing (Figure 7), maintaining most of E-cadherin in its unprocessed form (MW 120 kDa). GAPDH was used as a housekeeping gene for comparison purposes.

2.7 | Structure determination of inhibitory complexes

proBFT-3 is a two-lobed ~ 42 kDa zinc-dependent MP zymogen that is synthesized as a 397-residue preproprotein, including a signal peptide for secretion, a ~ 190 -residue pro-domain (PD; A¹⁸-R²¹¹) for folding and enzyme inactivation, and an approximately equally long CD (A²¹²-D³⁹⁷),

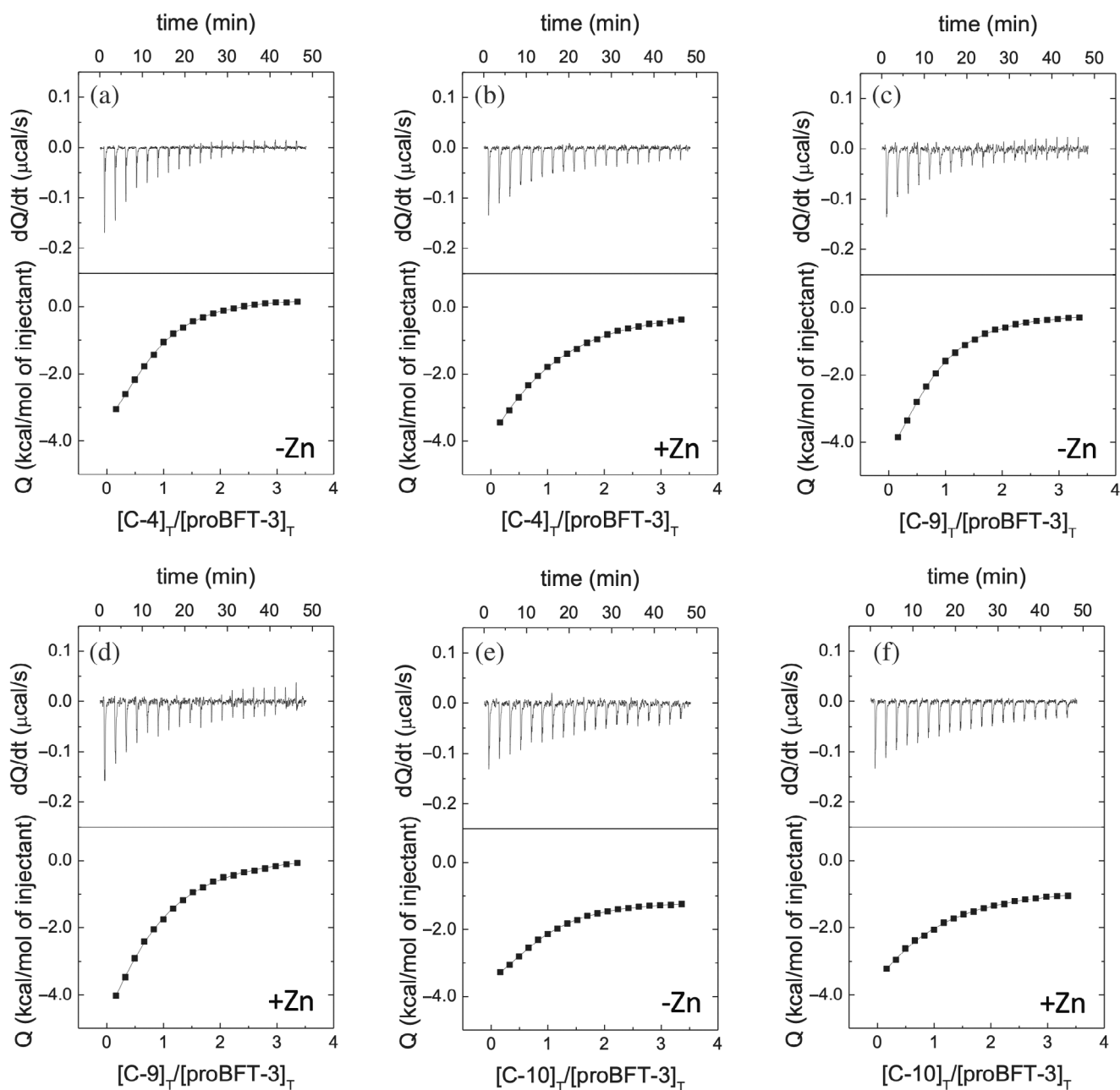


FIGURE 4 Interaction of selected compounds with proBFT-3. Calorimetric titrations for C-4 (a and b), C-9 (c and d) and C-10 (e and f) interacting with proBFT-3, in the absence (left) and the presence (right) of zinc. Thermograms (upper panels; thermal power required to maintain an almost zero temperature difference between sample and reference cell) and binding isotherms (lower panels; ligand-normalized heat effect per peak as a function of the molar ratio) are shown. Nonlinear fits according to a model considering a single ligand binding site (continuous lines) are shown

which belongs to the metzincin clan of metalloproteases.^{9,28} Importantly, the two globular entities of the PD and CD are connected by an inhibitory C-terminal linker segment of the PD (L¹⁸⁶-R²¹¹), which runs along the active-site cleft and binds to the CD in the opposite direction of a substrate. Via a so-called “aspartate-switch mechanism,”⁹ D¹⁹⁴ of the linker binds to the catalytic zinc ion, thereby displacing the active-site water and rendering the protease

inactive in its zymogenic form. The catalytic site is built by a consensus zinc-binding motif, namely HE³⁴⁹XXHXXGXXH, containing three zinc-binding histidine residues and a glutamate residue as the general base/acid for catalysis. The active site is further complemented by a loop segment and a tight 1,4- β -turn centered on M³⁶⁶, the so-called “Met-turn,” which forms a hydrophobic basement just underneath the catalytic zinc ion (Figure 8).

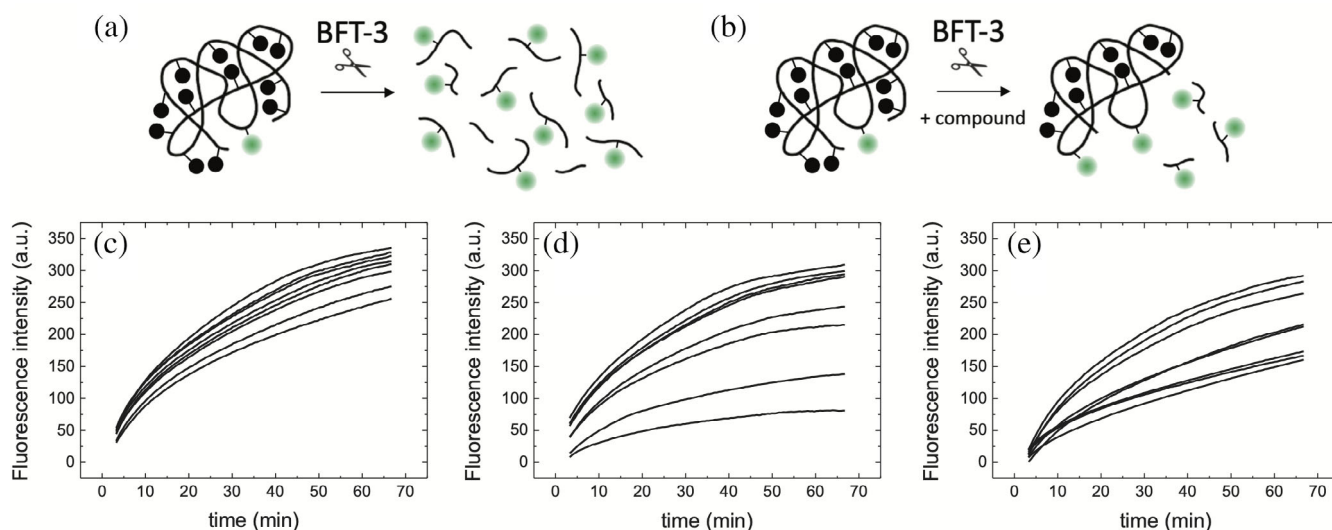


FIGURE 5 Proteolytic activity of BFT-3 measured *in vitro*, and inhibitory effect of selected compounds. (a and b) BODIPY FL casein was employed as a fluorescent substrate for trypsin-activated BFT-3. Loss of reciprocal fluorophore quenching due to proteolytic processing by BFT-3 results in an increase of fluorescence over time. (a) Maximal activity is observed with BFT-3; (b) Addition of an inhibitor compound reduces the hydrolytic rate, observing a lower fluorescence signal. (c–e) Increasing the concentration of the compounds (twofold serial dilutions from 1 to 0 mM) decreased the activity of BFT-3: (c) C-4, (d) C-9, and (e) C-10. While proBFT-3 showed no activity, trypsin yielded some signal at the used concentrations, but much lower than that of BFT-3, and its contribution was subtracted from the total signal of the trypsin-activated BFT-3 (Figure S1)

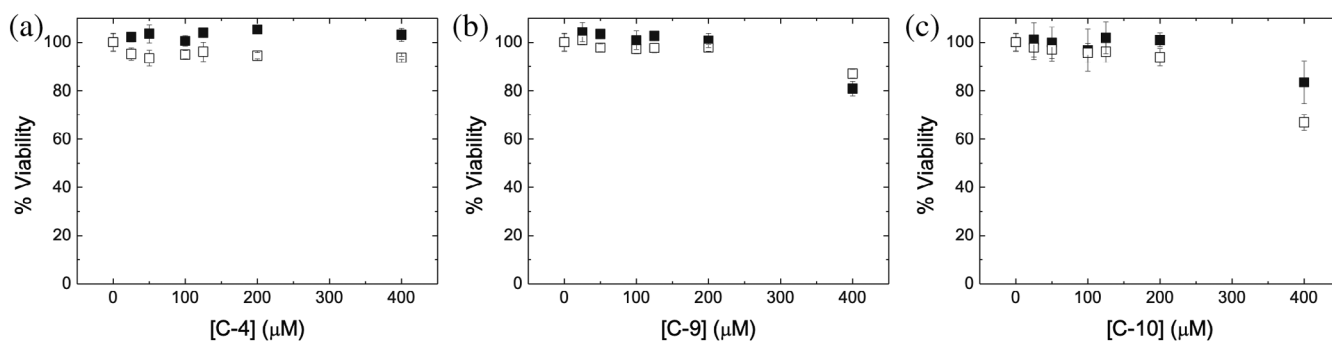


FIGURE 6 Cytotoxicity of compounds against HT-29 and HeLa cell lines. Cell viability values for HT-29 (open squares) and HeLa cells (filled squares) were determined by CellTiter 96[®] assay after 48 hr of incubation with increasing concentrations of (a) C-4, (b) C-9, and (c) C-10. All data are presented as the average \pm standard deviation of three biological replicates, performing the assay twice with technical replicates

We tested the most promising candidates from our biophysical and biochemical characterization for co-crystallization, namely C-4, C-9, and C-10, and succeeded for all three of them. Notably, all compounds bound in similar orientation into a prominent pocket at the top rear of the CD, where the inhibitors inserted wedge-like between the end of the so-called “adamalysin helix” ($\alpha 5$) and the first three strands ($\beta 12$, $\beta 13$, $\beta 14$) of the β -sheet of the upper subdomain (cf. left and a middle panel of Figure 9 and Figure S2). This binding was found consistently in the two protomer complexes present in all crystallographic asymmetric units. Importantly, while for C-9

(307.35 Da) and C-10 (302.29 Da) one inhibitor moiety was found at the exosite with interaction areas of 382 and 364 \AA^2 , respectively, two molecules of the smaller C-4 (261.26 Da) were bound, thereby increasing the interface from 304 \AA^2 for a single C-4 molecule to 497 \AA^2 . However, while the first C-4 molecule is deeply buried in the protein moiety, with only 14% of its surface being solvent accessible, the second one is found further outside with 43% of its surface solvent accessible. In comparison, for C-9 and C-10, 76% of the surfaces were buried by proBFT-3, which is highly similar to the combined 71% for the two C-4 molecules. However, our ITC data

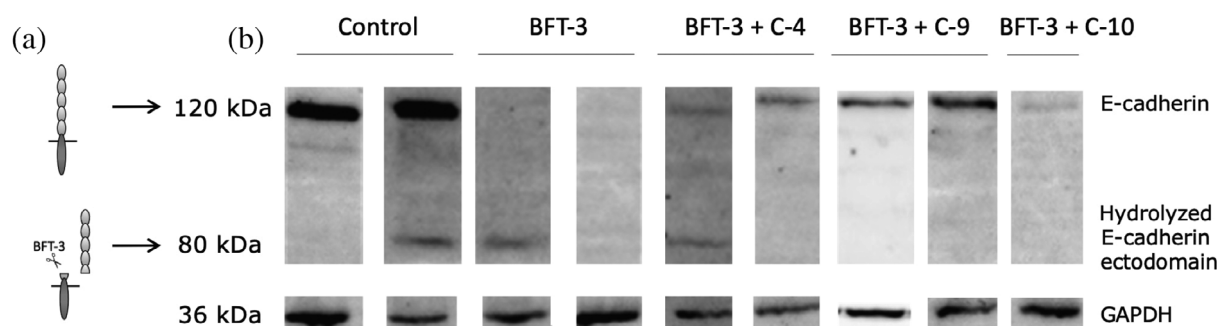


FIGURE 7 Proteolytic activity of BFT-3 and inhibitory effect of selected compounds monitored in a cell-based assay. (a) BFT-3 processing of E-cadherin (MW 120 kDa) results in the release of its ectodomain (MW 80 kDa). (b) In the absence of BFT-3, no degradation of E-cadherin was observed, whereas the presence of BFT-3 led to complete degradation of full-length E-cadherin, while the ectodomain was still partly detectable. The presence of compounds C-4, C-9, and C-10 at 120 μ M inhibited E-cadherin processing, as evident by detected western blot bands at 120 kDa. While proBFT-3 was added to the assay, proteases present in the cell culture medium, as well as self-activation, result in activated BFT-3 protein under these conditions

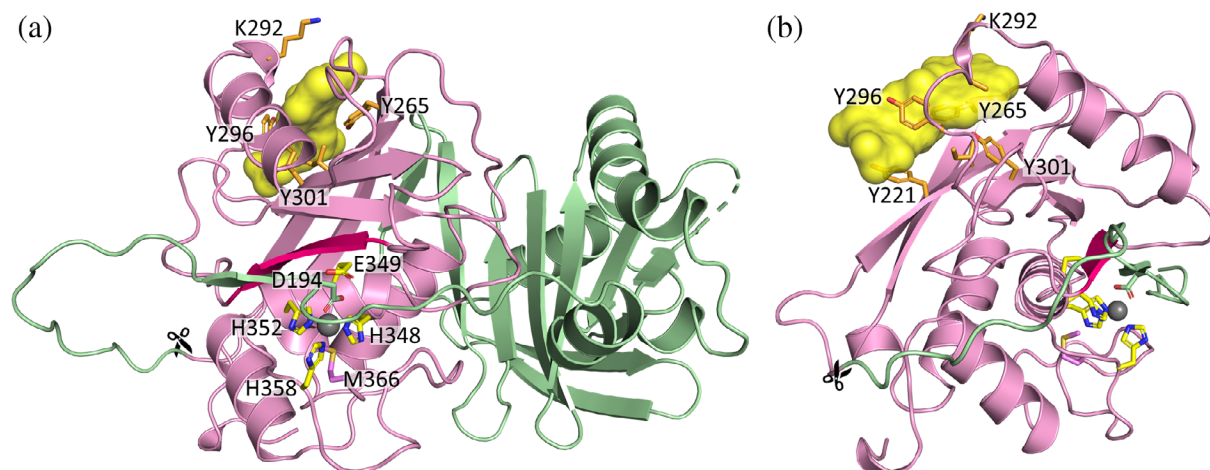


FIGURE 8 Crystallographic structure of proBFT-3 in complex with an identified inhibitor. (a) Overall structure in front view and (b) side view of proBFT-3. The prodomain (PD) and catalytic domain (CD) of unbound proBFT-3 (PDB 7PND) are shown as green and pink ribbons, with α -helices and β -strands as coiled ribbons and flat arrows, respectively. The active-site residues are depicted as sticks with yellow carbons, the catalytic zinc as a gray sphere, and the M³⁶⁶ of the hydrophobic basement is shown with violet carbon atoms. Of note, the linker segment of the PD binds to the CD in a reverse direction compared to a substrate, and the aspartate-switch D¹⁹⁴ is shown in stick mode with green carbons. The exosite responsible for inhibitor binding is located at the back rear of the CD, \sim 25 \AA away from the active site, and is depicted as a yellow semi-transparent surface resulting from the overlaid small-molecule inhibitors identified in this study extracted from PDB entries 7POL, 7POO, 7POQ, and 7POU, after superposing the respective proBFT-3 moieties. Key inhibitor-binding residues are shown as sticks with orange carbons. The substrate-guiding upper-rim strand of the CD is colored in hot pink, and the activation site of native BFT-3 is indicated with a scissor. The polypeptide chain is interrupted for segment S¹⁶¹-G¹⁶⁷ of the PD, as indicated by a dashed line. For the side view, PD residues Val³⁴-Asn¹⁸⁵ were omitted for clarity. Of note, corresponding molecular representations of all five determined X-ray structures, each with two protomers per asymmetric unit, are shown in Figure S2

showed no evidence for the second C-4 molecule, most likely due to the lower inhibitor concentrations used in the calorimetric experiment, implying a much higher affinity for the first binding event.

The main ligand interactions by proBFT-3 are performed with four tyrosines and a lysine residue (K²⁹²). Tyrosines Y²²¹, Y²⁶⁵, and Y³⁰¹ are located on β -strands β 12, β 13, and β 14, respectively, while Tyr²⁹⁶ is provided

by the loop after helix α 5. Together, they outline the ligand binding pocket and literally sandwich the bound ligands, with the lysine closing in from the top (Figure 9, left panel). Importantly, while the tyrosines nearly perfectly superimpose in both the non-ligated and complexed structures, the lysine sidechain closes the distance to the opposing side of the exosite cleft by nearly 2 \AA (measured between K²⁹²N ζ and T²⁶⁶C α ; see

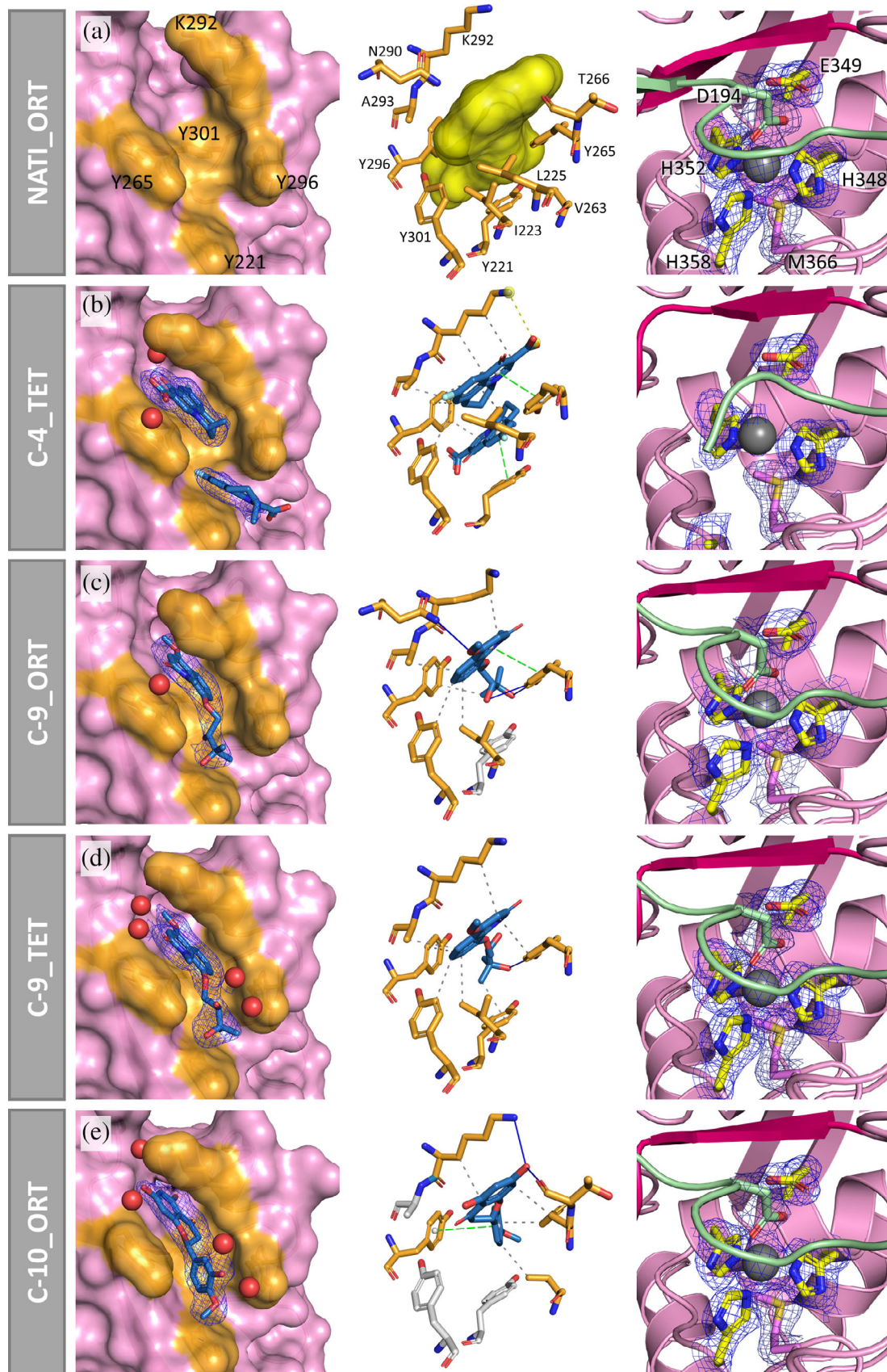


FIGURE 9 Legend on next page.

e.g., Figure S2). Additionally, while the tyrosines contribute with both hydrophobic and parallel π -stacking interactions to inhibitor binding, K²⁹² provides, in addition to hydrophobic interactions, a salt bridge and a hydrogen bond in the C-4 and C-10 complexes, respectively (Figure 9). Overall, the three compounds were found in similar orientation and performing analogous interactions (Figure S4) with the exception of the extended binding interface for C-4 due to the second inhibitory molecule. Ligand-omitted and bulk solvent-excluding mFo-DFc polder maps²⁹ were calculated using PHENIX,³⁰ contoured at 3.0 σ in Coot,³¹ and are shown for all exosite-binding inhibitory compounds in Figure S5.

Notably, inhibitor binding at the exosite appeared to impact protein crystallization. While the non-ligated proBFT-3 crystallized in the orthorhombic (ORTH) space group P2₁2₁2₁ and diffracted to 1.84 Å resolution, the complex structures with C-4 (1.95 Å), C-9 (1.84 Å), and C-10 (2.03 Å) all crystallized in the tetragonal (TETR) space group P4₁2₁2. For C-9, we further succeeded in obtaining an ORTH structure, but at a significantly lower resolution (2.70 Å). Intriguingly, the building block of both space groups, the crystallographic asymmetric unit, is protein-wise identical in both space groups, with two protomers packing back-to-back and a protein-protein interface area of $\sim 1,000$ Å². Biocomputational analysis of this surface with Protein Interfaces, Surfaces, and Assemblies software (PISA)³² indicated this surface was not relevant for dimerization. However, using size-exclusion chromatography, a concentration-independent monomer-dimer equilibrium was observed with significant interface stability based on

the immediate reinjection of the dimer peak (Figure S6). For crystallization experiments, both the monomeric and dimeric peaks were concentrated together. Of note, as the interface is largely built by the prodomains, the activated BFT-3 protein is unlikely to dimerize.

Importantly, inhibitor binding to the exosite profoundly impacted the binding of the catalytic zinc despite occurring ~ 25 Å apart. While the thermal displacement parameters of the active-site residues were only slightly lower in the inhibitor complexes than in the overall structure (-12%), this effect was more than double in the non-ligated structure (-26%), which indicates that inhibitor binding caused active-site destabilization. Similarly, when looking at the active-site zinc ion, we observed an increase in its thermal displacement parameters upon inhibitor binding, which was typically accompanied by a diminished metal occupancy. This impact was most pronounced in the C-4 complex structure, where the active site, especially H³⁵⁸, is distorted in both chains, and the zinc occupancy is reduced to 0.34 for chain A, and the metal is entirely missing in chain B (Figure 9 and Figure S2, right panels). A similar impact was observed for C-9 in the orthogonal space group, where the occupancy fell to 0.22 and 0.59 in chains A and B, respectively. Compared to non-ligated proBFT-3, a 3.3-fold lower occupancy of the zinc ion (calculated as the zinc b-factor normalized to full-occupancy divided by the overall b-factor of the structure) was identified. Even for C-10, where full zinc occupancy was observed, and for the TETR C-9 complex structure, zinc stability was reduced by $\sim 20\%$, despite little effect at first sight. At this point, it is important to note that all crystallization experiments

FIGURE 9 Binding of inhibitors to the newly identified exosite on proBFT-3. Close-up views of the inhibitor-binding exosite (left), the protein-ligand interaction network (middle), and the active site of the catalytic domain (CD) (right) in the distinct structures. Of note, chain A of the crystallographic asymmetric unit is depicted for each of the determined X-ray structures. The corresponding second protein molecule (chain B) is shown in Figure S2 with the same settings and orientations as shown here. Left: Back view onto the ligand-binding exosite. proBFT-3 is shown as a pink semi-transparent surface with key ligand-binding residues shown as sticks with orange carbons. The respective inhibitor is shown in sky-blue and stick mode, with the corresponding electron density map (2Fo-Fc) contoured at 1.0 sigma, and using a carve radius of 2.0 Å. Water molecules in hydrogen bond-forming distance (≤ 3.4 Å) are shown as red spheres. Middle: Protein-ligand interaction networks at the inhibitory exosite. The orientation is similar to the overview structure in Figure 8, and rotated $\sim 180^\circ$ away compared to the view of the figures on the left. Inhibitors are shown in atom-color mode with carbons in sky blue. In (a), the exosite of unligated proBFT-3 is shown, but, as in Figure 8, complemented with the cumulative surface of all crystallized inhibitors in yellow. (b) For C-4 (PDB entry: 7POL), two copies of the inhibitor were found at each exosite. For C-9, two crystal forms were identified: (c) orthorhombic (ORTH; PDB entry: 7POO) and (d) tetragonal (TETR; PDB entry: 7POQ). The ligand interaction network for C-10 (PDB entry: 7POU) is shown in (e). All protein-ligand interactions were calculated using the PLIP webserver 43, and are displayed as gray, green, and yellow dashed lines for hydrophobic interactions, parallel π -stacking, and salt bridges, respectively, while hydrogen bonds are depicted as solid blue lines. Right: Active-site views of proBFT-3 in the non-ligated and inhibitor-complexed structures. A similar orientation as in Figure 8 is shown, with the same key active-site residues depicted in stick mode. The molecular representation was overlaid with the corresponding electron density map (2Fo-Fc) contoured at 1.0 sigma, and using a carve radius of 2.0 Å. Importantly, the active site of C-4-complexed proBFT-3 is completely perturbed, highlighted by a low zinc occupancy and missing electron density for the third proteinaceous zinc ligand (H358), despite the presence of 5 μ M ZnCl₂ in the protein buffer.

were carried out in the presence of 5 μM ZnCl_2 . As a result, zinc occupancy in solution may be even lower. This is consistent with the fact that the tested compounds were first identified against zinc-free (EDTA-treated) proBFT-3, their higher affinity toward the zinc-free conformational state, and the observed competitive interplay between compound binding at the identified exosite and zinc occupation at the catalytic site.

3 | DISCUSSION

Depending on their functional role, protein-bound zinc ions can be classified as either structural (i.e., stabilizing the folded protein) or catalytic (i.e., involved in an enzymatic process). While the former ones are typically bound distal from the active site and coordinated by cysteine residues (e.g., HCV NS3 protease), the latter ones are primarily complexed by aspartates, glutamates, and histidines (e.g., H^{348} , H^{352} , and H^{358} in BFT-3) at the active center. However, the latter may also contribute to the overall stability of the protein in addition to facilitate catalysis. Due to differences in the respective coordination spheres, EDTA readily abstracts zinc from BFT-3 at pH 7, but fails to do so in HCV NS3 at pH >6,³³ despite EDTA having a picomolar binding affinity for zinc.^{34,35} Importantly, we detected considerable unfolding in proBFT-3 upon zinc removal, albeit to a lesser extent than in cc NS3,²⁶ and moderate changes were observed in both the secondary structure content (in fact, an unexpected increase in ellipticity) and the intrinsic tryptophan fluorescence. This may be explained by zinc acting as an anchor between the upper and lower halves of the proBFT-3 CD, so that its depletion leads to increased overall protein flexibility while having little impact on the secondary structure content and the tryptophan environment. Indeed, in the absence of zinc, the solvent-exposed surface area increased significantly, as evidenced by an increase in ANS fluorescence quantum yield. In contrast, both the unfolding stability and cooperativity decreased, as reflected by the much lower thermal stability of the protein (lower unfolding temperature and enthalpy), thus confirming that the catalytic zinc ion serves also a critical structural role in proBFT-3. In fact, based on the thermal stability parameters obtained in DSF (Figure 2), an estimated stabilization Gibbs energy of ~ 3.6 kcal/mol can be attributed to the zinc interaction, which is significantly higher than the intrinsic stabilization energy of the zinc-free state (~ 2.5 – 3.0 kcal/mol), and accounts for $\sim 60\%$ of the total proBFT-3 stabilization energy.

Thus, we postulate that BFT-3 is a conditionally disordered protein (CDP), as previously shown for HCV NS3.³⁶ CDPs function by temporarily adopting a well-folded structure but are otherwise partially or completely disordered. This conformational switch represents a regulatory element that can be triggered by a post-translational modification, interaction with a biological partner, or a change in environmental conditions (e.g., zinc levels). Notably, CDPs have low structural stability and show properties similar to intrinsically disordered proteins as they populate conformational states separated by small conformational energy gaps. In case of (pro)BFT-3, the solvent and the protein alone seem insufficient to drive the folding toward the structured state. However, upon zinc binding, the required interactions and structural context are available. Importantly, the tight spatial, thermodynamic, and kinetic regulation of the intracellular zinc pool at subnanomolar levels,^{37–40} the required proBFT-3 plasticity for secretion into the gut lumen (i.e., the protein can adopt a sufficiently relaxed structure to undergo membrane translocation and refold afterwards), and the rather low intrinsic conformational stabilization Gibbs energy of proBFT-3, support the notion that the partially unfolded zinc-free state of proBFT-3 is indeed of physiological importance. This may add an extra layer of proBFT-3 activity regulation on top of the inhibitory function of the PD. While the partially unfolded state due to zinc scarcity would ensure negligible intracellular proBFT-3 activity, its structural plasticity could expedite both protein secretion and activation—likely by a host protease such as trypsin. Nonetheless, enhanced and durable BFT-3 activity would be attainable in the gut lumen upon zinc binding and stabilization of the protein. This conceivable physiological relevance of proBFT-3's zinc-free state prompted us to search for small molecules capable of binding and stabilizing this partially disordered conformation. This would trap the protein in an inactive state by an allosteric inhibition mechanism where ligand binding modulates the conformational equilibrium between the active and inactive state.^{41,42} Such a resulting inhibition mechanism can be classified as either competitive or mixed-inhibition depending on whether the substrate and inhibitor are mutually exclusive (i.e., the substrate and inhibitor solely interact with the folded and partially unfolded protein, respectively), or if a ternary complex is possible and retains reduced but evident activity.

We were able to identify 11 known drugs from the Prestwick Chemical Library as potential BFT-3 ligands using a thermal shift assay (TSA)-based screening procedure under experimental conditions favoring zinc dissociation (i.e., in the presence of the chelating agent EDTA)

and a semi-quantitative YES/NO readout for hit selection. Subsequently, since TSA analysis only provides indirect evidence for ligand interaction, and as the identified stabilization cannot be directly translated into binding affinities (as it additionally depends on [free] ligand concentration, ligand binding enthalpy, and binding heat capacity⁴³), we conducted ITC experiments to assess target engagement and to determine actual binding affinities. Furthermore, we evaluated the biological effect of the compounds using both in vitro and cell-based assays.

While several initial hit compounds lacked adequate binding affinity, C-4, C-9, and C-10 demonstrated significant (pro)BFT-3 binding (i.e., a K_d in the micromolar range) and inhibitory efficacy in both cell-based E-cadherin processing assays and in vitro cleavage studies using BODIPY-casein. Notably, the identified compounds bound to both the proBFT-3 zymogen and the active BFT-3 protein, and interacted with both the zinc-free and zinc-bound form, albeit with reduced affinity for the latter (see Figure 4 and Table 1). Intriguingly, the less favorable Gibbs energy of binding to the zinc-bound enzyme was accompanied by a more favorable enthalpic interaction but which was outweighed by a less favorable (or more unfavorable) entropic term. Importantly, this competitive interplay between the active-site metal (and thus fully folded protein) and the identified inhibitors (which favor the zinc-free partially unfolded state) is also reflected in the reduced zinc occupancy in the determined crystal structures of the complexes—remarkably even despite the presence of 5 μM ZnCl_2 during crystallization. The crystal structures also explained the similar affinities to the active and zymogen form as the identified exosite is located on the opposite face of the CD and thus distal to the PD. Crucially, as the identified compounds bind to both zinc-free and zinc-bound BFT-3, their overall inhibitory activity may rely on a combined (a) indirect reciprocal (i.e., substrate and inhibitor reciprocally exclude themselves by preferentially interacting with different BFT-3 zinc-ligation macrostates, namely zinc-bound and the zinc-free BFT-3, respectively) and (b) direct reciprocal competitive effect (i.e., substrate and inhibitor exclude themselves reciprocally by interacting with different conformational microstates of the same macrostate, where the inhibitor distorts the catalytic process and hinders substrate binding and/or catalysis). Consequently, the apparent inhibitory effect will depend on the compound's ability to alter the thermodynamics of the enzyme-substrate interaction (i.e., increase in K_m) and dynamics (i.e., decrease in V_{max}), and the residual activity of the ternary enzyme-substrate-inhibitor complex (ideally negligible). In a simple mixed inhibition scheme, the apparent K_m and V_{max} at a certain inhibitor concentration $[I]$ are given by:

$$\begin{aligned} K_m^{\text{app}} &= K_m \frac{1 + \frac{[I]}{K_i}}{1 + \frac{[I]}{\alpha K_i}}, \\ V_{\text{max}}^{\text{app}} &= V_{\text{max}} \frac{1 + \beta \frac{[I]}{\alpha K_i}}{1 + \frac{[I]}{\alpha K_i}}, \end{aligned} \quad (1)$$

where K_i and αK_i are the inhibition constants for the substrate-free enzyme (equivalent to the dissociation constant of the enzyme-inhibitor complex) and the substrate-bound enzyme (equivalent to the dissociation constant of the enzyme: substrate-inhibitor interaction, with $\alpha < 1$ and $\alpha > 1$ reflecting positive and negative substrate-inhibitor cooperativity, respectively), and β accounting for the residual activity of the ternary complex. At very high inhibitor concentration, this becomes:

$$\begin{aligned} K_m^{\text{app}} &= K_m \alpha \\ V_{\text{max}}^{\text{app}} &= V_{\text{max}} \beta \end{aligned} \quad (2)$$

Consequently, a non-zero β factor results in incomplete inhibition even at high inhibitor concentrations. In fact, this is what we observed despite a clear dose-response effect in the in vitro inhibitory experiments (see Figure 5). However, the heterogeneity of the substrate BODIPY-casein complicates interpretation due to the presence of many different cleavage sites at varying quantities, resulting in a complex behavior of both enzyme and inhibitor. Thus, we verified the inhibitory capacity of the selected compounds in a cell-based assay by monitoring E-cadherin processing. The three compounds (C-4, C-9, and C-10) diminished the efficacy of BFT-3 for cleaving E-cadherin (see Figure 7) at concentrations lower than their estimated CC_{50} (see Figure 6).

Furthermore, additional evidence for target engagement and the allosteric mode of inhibition was obtained by X-ray crystallography. Obviously, crystallization of the partially unfolded zinc-free (pro)BFT-3 would be impossible, potentially explaining the need of ZnCl_2 for crystallization. But as the identified compounds also bind to the zinc-bound state of (pro)BFT-3, we eventually succeeded in the determination of the complex structures with all three compounds (C-4, C-9, and C-10). The structures revealed that the ligands bound into the same pronounced pocket at the upper rear of the CD. Notably, despite the exosite being located away from the active site, inhibitor binding leads to a destabilization of the active site, as evidenced by reduced zinc occupancies and increased temperature factors.

To conclude, BFT-3, together with the other two isoforms BFT-1 and BFT-2, is the only known virulence factor in ETBF, causing barrier disruption and inflammation of the colon during infection, and it is over-expressed in the mucosa of inflammatory bowel disease and colorectal cancer patients. Using extensive compound screening, biophysical assays, in vitro and cell-based activity assays, and X-ray crystallography, we identified three FDA-approved small molecule drugs, namely flumequine (C-4), foliosidine (C-9), and hesperetin (C-10), that target and inhibit BFT-3 in a dose-dependent manner. They show great promise to be either directly repurposed for preventive or therapeutic treatment of *B. fragilis* chronic infection, diminishing the risk of inflammation and colorectal cancer development, or, given their small molecular mass, to be further optimized to improve their affinity, selectivity, or bioavailability.

4 | MATERIALS AND METHODS

4.1 | Protein expression and purification

The proBFT-3 enterotoxin precursor (residues A¹⁸-D³⁹⁷; UniProt access code O86049) was cloned in the pET-28-based pCri-8a expression vector,⁴³ which attaches a fusion protein with a TEV-cleavable N-terminal His₆-tag.⁹ Small-scale *E. coli* BL21 (DE3) cell cultures were grown in LB/kanamycin (50 µg/ml) at 37°C overnight and used to inoculate large-scale 6-L cultures of LB/kanamycin (50 µg/ml), which were incubated at 37°C until OD₆₀₀ ≈ 0.6. Protein expression was induced with 1 mM isopropyl 1-thio-β-D-galactopyranoside at 18°C overnight. Cells were harvested by centrifugation at 4°C for 10 min at 20,000g in an Avanti J-26 XP Centrifuge (Beckman Coulter) and resuspended in lysis buffer (500 mM NaCl, 20 mM Tris-HCl, pH 7.4). Cells were lysed by sonication (Sonic Vibra-Cell Ultrasonic Liquid Processor) on ice, after adding 20 U/ml benzonase (Merck-Millipore) and 0.5 mg/ml lysozyme (Carbosynth). Cell debris was removed by centrifugation at 4°C for 10 min at 10,000g. Supernatants were clarified by subsequent filtration (0.45 µm-pore membrane) and subjected to affinity chromatography purification in an ÄKTA FPLC System (GE Healthcare Life Sciences) using a cobalt HiTrap TALON column (GE Healthcare Life Sciences) and applying an imidazole gradient (10–250 mM). Purity was assessed by SDS-PAGE, and pure protein fractions were pooled and dialyzed to remove imidazole (150 mM NaCl, Tris-HCl 20 mM, pH 7.4). Protein concentration was quantified using the theoretical extinction coefficient (54,780 M⁻¹/cm) at 280 nm. Zinc-free protein was obtained by adding EDTA at a concentration not

higher than 1 mM. Whenever required, mature active BFT-3 was obtained from proBFT-3 by activation with trypsin (PAN-Biotech GmbH) added at a 1:100 mass ratio and incubated at room temperature for 3 hr.

4.2 | CD and fluorescence spectrometry

Circular dichroism spectra were recorded in a thermostated Chirascan spectrometer (Applied Photophysics), using a quartz cuvette of 0.1-cm path length (Hellma Analytics) and selecting a bandwidth of 1 nm, a spectral resolution of 0.5 nm, and a response time of 5 s. Temperature was controlled by a Peltier unit and monitored using a temperature probe. Assays were performed in the far-UV range (190–260 nm). Protein concentration was set to 10 µM.

Fluorescence spectra were collected in a Cary Eclipse spectrofluorometer (Agilent) interfaced with a thermostated multicell holder (Peltier). The slit widths were 5 nm for both excitation and emission wavelengths. An extrinsic probe (8-anilino-1-naphthalene sulfonic acid, ANS) was employed to assess the solvent-exposed molecular surface, using an excitation wavelength of 370 nm and recording the emission spectrum from 400 to 600 nm. Assays were carried out at 25°C in a quartz cell of 1-cm path length (Hellma Analytics). proBFT-3 concentration was set to 2 µM and ANS concentration was set to 100 µM. All measurements were performed in 150 mM NaCl, 20 mM Tris-HCl, pH 7.0, without or with 1 mM EDTA to remove the catalytic zinc from the protein.

4.3 | Differential scanning fluorimetry

The thermal stability of proBFT-3 and its modulation by zinc binding was assessed by DSF in a Mx3005p real-time qPCR device (Agilent). The fluorescence emission intensity of the extrinsic fluorophore SYPRO Orange Protein Gel Stain (Thermo Fisher Scientific) was recorded as a function of temperature in 150 mM NaCl, 20 mM Tris-HCl, pH 7.0, at a scanning rate of 1°C/min using an excitation and an emission wavelength filter of 496 and 610 nm, respectively. These were the closest available to the theoretical values of the fluorophore (491 and 586 nm). SYPRO Orange binds to solvent-exposed hydrophobic patches on the protein surface upon protein unfolding, thusly undergoing a fluorescence quantum yield enhancement with increase of the fluorescence intensity.^{43–45} In order to deplete the protein of zinc and get the apozymogen or apoenzyme, 200 µM EDTA was added. Data analysis of the experimental data considered

a single unfolding transition model and provided relevant thermodynamic stability parameters, viz. the unfolding temperature, T_m , and the associated unfolding enthalpy, $\Delta H(T_m)$.

4.4 | Chemical library

The Prestwick Chemical Library (Prestwick Company), consisting of a set of 1,120 FDA-approved drugs selected for providing large chemical and pharmacological diversity, was supplied with compounds dissolved in 100% dimethyl sulfoxide (DMSO) at a concentration of 4 mM. Information on their bioavailability, as well as toxicity and safety in humans, is available from the manufacturer.

4.5 | Experimental ligand screening

Potential ligands for proBFT-3 were identified from the Prestwick Chemical Library following an experimental screening procedure based on the TSA by DSF, which detects ligand-induced protein stabilization against thermal denaturation,^{44–47} in a FluoDia T70 fluorescence microplate reader (Photon Technology International). The procedure was similar to that employed previously for identifying small-molecule inhibitors of *Helicobacter pylori* flavodoxin⁴⁸ and the intrinsically disordered DNA-binding protein NUPR1,⁴⁹ as well as to find pharmacological chaperones for human phenylalanine hydroxylase.⁵⁰ Furthermore, as proBFT-3 is a zinc-dependent protein, we employed a modified version of the screening procedure tailored to the identification of potential ligands of the zinc-free conformational state as previously described for the NS3 protease from hepatitis C virus.²⁶ Briefly, 100 μ l volumes containing 1 μ M proBFT-3, 100 μ M tester compound, and 1X SYPRO Orange in 150 mM NaCl, 5 mM EDTA, 20 mM Tris-HCl, pH 7.4 were dispensed into 96-well microplates (ThermoFast 96 skirted plates, Thermo Scientific). Each reaction volume contained 2.5% DMSO from the tester stock solutions. Thus, control samples of proBFT-3 with 2.5% DMSO were routinely included in each microplate. Solutions were overlaid with 20 μ l mineral oil to prevent evaporation and incubated at 25°C for 30 min. Thermal unfolding curves were registered from 25 to 75°C in 1°C steps by monitoring the fluorescence. We used excitation and emission wavelength filters (470 and 570 nm, respectively) that were the closest available to the theoretical values of the fluorophore (491 and 586 nm). Thermal equilibrium was achieved at each temperature by accounting for an equilibration time of 1 min before each

measurement, which corresponded to an operational heating rate of $\sim 0.25^\circ\text{C}/\text{min}$. Hits were identified as those increasing the temperature unfolding temperature T_m at least 3°C compared to the internal controls in each microplate.

4.6 | Isothermal titration calorimetry

The interaction of selected compounds with proBFT-3 was assessed with a high-sensitivity isothermal titration calorimeter Auto-iTC200 (MicroCal, Malvern-Panalytical). Experiments were performed at 25°C in 150 mM NaCl, 20 mM Tris-HCl, pH 7.4, and 1 mM EDTA was added for experiments with zinc-free protein. The protein solution at $\sim 20 \mu\text{M}$ was titrated in the calorimetric cell with compound solution at $\sim 300 \mu\text{M}$ through a series of 19 injections of 2 μl , with a stirring speed of 750 rpm and a reference power of 10 $\mu\text{cal/s}$. The heat evolved after each ligand injection was obtained from the integration of the calorimetric signal. The heat due to the binding reaction was obtained as the difference between the reaction heat and the corresponding heat of dilution, the latter estimated as a constant value throughout the experiment, and included as an adjustable parameter in the analysis. Control experiments (compound injected into buffer) were performed under the same experimental conditions in order to observe potential unspecific phenomena (e.g., solution composition mismatches or self-association of compounds). The enthalpy change, ΔH , and the association constant, K_a , of the binding reaction were obtained through nonlinear least-squares regression data analysis of the experimental data applying a model considering a single ligand binding site in the protein. Uncertainties for estimated parameters were calculated according to asymmetric profile likelihood confidence intervals.⁵¹ Experiments were performed in replicates and data were analyzed using in-house developed software implemented in Origin 7 (OriginLab).

4.7 | In vitro inhibition of BFT-3 activity

To evaluate the activity of BFT-3 and the inhibitory effect of the tester compounds, proteolytic assays were performed using BODIPY-casein as the substrate (EnzChek Protease Assay Kit; Thermo Fisher Scientific) according to the manufacturer's instructions. Briefly, proBFT-3 at a concentration of 3 μM in 150 mM NaCl, 20 mM Tris-HCl, pH 7.4, was first activated by adding trypsin (PAN-Biotech GmbH) at a 1:100 M ratio in a final volume of 50 μl and incubated for 3 hr at room temperature. Then, twofold serial dilutions of each compound were made

from an initial concentration of 3 mM compound in 7% DMSO, 0.1 mM NaN_3 , 10 mM Tris-HCl, pH 7.8, and 50 μl of each dilution were added to the protein sample and subsequently incubated for 1–2 hr. Subsequently, 50 μl substrate were added to each protein-compound sample, and the fluorescence intensity was recorded (excitation/emission: 492/516 nm, the available wavelengths closer to the recommended 505/513 nm for the substrate) for 1 h at 37°C in a Stratagene Mx3005P Real-time PCR instrument (Agilent Technologies). Control experiments featuring proBFT-3 without trypsin activation, trypsin, and buffer alone were performed under the same experimental conditions.

4.8 | Cell viability assays

Cellular cytotoxicity of the selected compounds was assessed in HT-29 (human colon adenocarcinoma) and HeLa (human cervix epithelioid carcinoma) cells obtained from ATCC and maintained in Dulbecco's Modified Eagle's Medium (DMEM; PAN-Biotech GmbH) supplemented with 10% FBS (Fetal Bovine Serum), 1% penicillin/streptomycin, and 1% NEAAs (non-essential amino acids) at 37°C with 5% CO_2 . Cells were plated and incubated for 48 hr in 96-well plates (8,000 cells in 100 μl per well for HeLa cells; 9,000 cells in 100 μl per well for HT-29 cells) with FBS-supplemented DMEM without phenol red (PAN-Biotech GmbH). Twofold serial dilutions of compounds were added to the cells up to a maximal concentration of 400 μM and incubated for 48 hr. The cytotoxicity, measured as cell viability, was assayed with the CellTiter 96 Aqueous One Solution Cell Proliferation Assay Kit (Promega). To this aim, 20 μl of CellTiter buffer, diluted 1:4 in FBS-supplemented DMEM without phenol red, were added to each well of the 96-well assay plates containing the samples. The plates were incubated at 37°C for 2 hr in humidified atmosphere with 5% CO_2 , and absorbance was recorded at 490 nm, with background correction at 800 nm. The readout was directly proportional to the number of living cells in the culture. Each condition was assayed in triplicate and experiments were repeated at least two times.

4.9 | In cell BFT-3 activity inhibition

Western-blot assays were performed to detect E-cadherin in cell samples to monitor the inhibitory capacity of tester compounds on processing by proBFT-3. HT-29 cells were seeded in 24-well plates (90,000 cells in 500 μl per well) with FBS-supplemented DMEM without phenol red. After 48 hr, proBFT-3 was incubated with or without

tester compounds in phosphate-buffered saline (PBS) for 3 hr. Then, DMEM without phenol red was added to the sample to a final proBFT-3 concentration of 25 nM. Cell media was removed from each well and the proBFT-3 or proBFT-3/compound solution was added to the cell culture. Of note, in the absence of inhibitor, proBFT-3 is expected to be either activated autoprotoleolytically or by a secreted protease from the cells. After 24 hr, cell lysates were obtained using cold radioimmunoprecipitation assay buffer (RIPA), which contains inhibitors of proteases and phosphatases. Samples were incubated on ice for 15 min to obtain protein extracts, which were diluted into Laemmli loading buffer. Samples were heated to 95°C for 5 min and subjected to 10% SDS-PAGE in a Mini-PROTEAN system (Bio-Rad) operated at 140 V. Proteins were transferred to a PVDF membrane using Mini-PROTEAN adaptors under wet and cold conditions at 400 mA for 60 min. Membranes were then blocked with 5% non-fat dry milk in Tris-buffered saline (TBS) at room temperature for 1 hr and incubated overnight at 4°C with the respective primary antibody (E-cadherin Antibody or GAPDH Antibody, Table S1), previously diluted 1:2,500 with blocking solution supplemented with 0.1% Tween 20 (TBS-T). After three washes with TBS-T, membranes were incubated with the secondary antibody (previously diluted 1:10,000 with TBS-T), which was marked with Alexa Fluor Plus 647 (Table S1) fluorescence label, at room temperature during 1 hr. After three further washes, the signal was recorded in a ChemiDoc Gel Imaging System (Bio-Rad).

4.10 | Protein crystallization

proBFT-3 protein was concentrated to 10–15 mg/ml using Vivaspin 20 centrifugal concentrators of 10-kDa molecular-mass cutoff (Sartorius, PES), and polished using a Superdex S200 gel filtration column connected to an ÄKTA Purifier 10 (GE Healthcare Life Sciences) with 50 mM NaCl, 20 mM Tris-HCl, pH 8.0, as running buffer. Peak fractions were pooled and re-concentrated to ~10 mg/ml, flash frozen in liquid nitrogen as 50- μl aliquots, and stored at –80°C until further use. High-throughput crystallization screenings were performed using a Phoenix dispenser robot (Art Robbins Instruments) in sitting-drop vapor-diffusion setup by mixing 100 nl of protein with 100 nl of reservoir solution. Commercial crystallization screens including JCSG+, PACT Premier, BCS, and LFS (all from Molecular Dimensions), and PEGRX, SaltRX, and Index Screen (all from Hampton Research) were used in duplicate setups to allow for incubation at 20 and 4°C in Bruker AXS Crystal Farms. Initial crystallization hits were subsequently optimized by hand and upscaled to 0.5- μl drops using standard

two-dimensional grid screening in sitting-drop vapor diffusion format.

Suitable crystals of unbound proBFT-3 in a new ORTH space group (NATI_ORTH) and in complexes with inhibitors C-4, C-9, and C-10 in ORTH or TETR space groups were obtained at 4°C from drops of 0.5 µl of protein solution (at 7.9 mg/ml in 50 mM sodium chloride, 20 mM Tris-HCl, pH 8.0, supplemented with 5 µM ZnCl₂ and 400 µM of the respective inhibitor) and 0.5 µl of reservoir solution. The final crystallization conditions were 18% PEG 3350, 0.2 M MgHCOO, pH 5.9 for NATI_ORTH; 20% PEG 3350, 0.2 M (NH₄)₂SO₄ for the C-4 TETR complex; 14% PEG 3350, 0.2 M MgCl₂, and 25% PEG 3350, 0.1 M Bis-Tris, pH 5.5, 0.2 M NH₄CH₃COO, for the C-9 TETR and ORTH complexes, respectively; and 22% PEG 3350, 0.1 M Bis-Tris-HCl, pH 5.5, 0.2 M (NH₄)₂SO₄ for the C-10 TETR complex. All crystals typically appeared within 7 days, contained two molecules per asymmetric unit, and were harvested and cryoprotected by soaking for 15–30 s in mother liquor supplemented with 2.5 M L-proline and 1 mM of the respective inhibitor. Of note, all inhibitor stocks were originally at 20 mM in 100% DMSO. Thus, crystallization conditions and cryoprotection buffers contained 2% and 5% DMSO, respectively, in all cases.

4.11 | Structure determination and analysis

Complete diffraction datasets of unbound and inhibitor-bound proBFT-3 crystals were collected at beamlines i04-1 and XALOC of the Diamond and ALBA synchrotrons, respectively. Data were integrated, scaled, merged, and reduced using XDS⁵² and XSCALE,⁵³ and transformed with XDSCONV to the reflection file format MTZ for use by the PHENIX,³⁰ BUSTER/TNT,⁵⁴ and CCP4⁵⁵ program packages. Structures were solved by molecular replacement using PHASER⁵⁶ with one protomer of Protein Data Bank (PDB) entry 3P24⁹ as a search model. Data collection and processing statistics are listed in Table S2. Protein-ligand interactions were analyzed using the PLIP web tool with default settings,^{57,58} and both protein–protein and protein-ligand interaction areas were calculated using the PDBePISA webserver.³¹ Molecular graphics representations were created using an open-source build of PYMOL version 2.5 Plus: The PyMOL Molecular Graphics System, (Version 2.5 Schrödinger, LLC).⁵⁹

AUTHOR CONTRIBUTIONS

Ana Jimenez-Alesanco: Data curation (equal); formal analysis (equal); investigation (equal); software (equal); validation (equal); writing – review and editing (equal).

Ulrich Eckhard: Data curation (equal); formal analysis (equal); investigation (equal); software (equal); validation (equal); visualization (equal); writing – review and editing (equal). **Marta Asencio del Rio:** Data curation (equal); formal analysis (equal); investigation (equal); writing – review and editing (equal). **Sonia Vega:** Investigation (equal); writing – review and editing (equal). **Tibisay Guevara:** Investigation (equal); writing – review and editing (equal). **Adrian Velazquez-Campoy:** Conceptualization (equal); formal analysis (equal); funding acquisition (equal); methodology (equal); resources (equal); software (equal); supervision (equal); writing – original draft (equal); writing – review and editing (equal). **Francesc Xavier Gomis-Rüth:** Conceptualization (equal); formal analysis (equal); funding acquisition (equal); resources (equal); software (equal); supervision (equal); writing – original draft (equal); writing – review and editing (equal). **Olga Abian:** Conceptualization (equal); formal analysis (equal); funding acquisition (equal); methodology (equal); resources (equal); software (equal); supervision (equal); writing – original draft (equal); writing – review and editing (equal).

ACKNOWLEDGMENTS

This study was supported by Miguel Servet Program from Instituto de Salud Carlos III (grant CPII13/00017), Fondo de Investigaciones Sanitarias from Instituto de Salud Carlos III, and European Union (ERDF/ESF, “Investing in your future”) (grant PI18/00349 and PI21/00394), Spanish Ministry of Economy and Competitiveness (grant BFU2016-78232-P), Diputación General de Aragón Pre-doctoral Research Contract 2019, Diputación General de Aragón Protein Targets and Bioactive Compounds Group E45_20R and Digestive Pathology Group B25_20R, Centro de Investigación Biomédica en Red en Enfermedades Hepáticas y Digestivas—CIBERehd, Spanish Ministry of Science and Innovation (grant PID2019-107725RG-I00), and Catalan Agency (grant 2017SGR3), Fundació “La Marató de TV3” (grant 201815), Secretary of Universities and Research and European Union Horizon 2020 COFUND program, Beatriu de Pinós post-doctoral fellowship. We are grateful to Xandra Kreplin and Joan Pous from the IBMB-CSIC High-Throughput Crystallography Platform for assistance with crystallization experiments, and we would like to thank Diamond Light Source and ALBA Synchrotron for beamtime allocation, and the staffs at beamlines i04-1 and XALOC for superb support with X-ray diffraction data collection.

DATA AVAILABILITY STATEMENT

The data that support the findings of this study are available from the corresponding author upon reasonable request.

ORCID

Adrian Velazquez-Campoy  <https://orcid.org/0000-0001-5702-4538>

Francisc Xavier Gomis-Rüth  <https://orcid.org/0000-0002-6848-6874>

REFERENCES

- Wexler HM. *Bacteroides*: The good, the bad, and the nitty-gritty. *Clin Microbiol Rev.* 2007;20:593–621.
- Wu S, Rhee KJ, Albesiano E, et al. A human colonic commensal promotes colon tumorigenesis via activation of T helper type 17 T cell responses. *Nat Med.* 2009;15:1016–1022.
- Sears CL. Enterotoxigenic *Bacteroides fragilis*: A rogue among symbiotes. *Clin Microbiol Rev.* 2009;22:349–369.
- Majid M, Andleeb S. Designing a multi-epitopic vaccine against the enterotoxigenic *Bacteroides fragilis* based on immunoinformatics approach. *Sci Rep.* 2019;9:1–15.
- Goldstein EJC. Anaerobic bacteremia. *Clin Infect Dis.* 1996;23:97–101.
- Biondi A, Basile F, Vacante M. Familial adenomatous polyposis and changes in the gut microbiota: New insights into colorectal cancer carcinogenesis. *World J Gastrointest Oncol.* 2021;13:495–508.
- Franco AA, Mundy LM, Trucksis M, Wu S, Kaper JB, Sears CL. Cloning and characterization of the *Bacteroides fragilis* metalloprotease toxin gene. *Infect Immun.* 1997;65:1007–1013.
- Chung G-T, Franco AA, Wu S, et al. Identification of a third metalloprotease toxin gene in extraintestinal isolates of *Bacteroides fragilis*. *Infect Immun.* 1999;67:4945–4949.
- Goulas T, Arolas JL, Gomis-Rüth FX. Structure, function and latency regulation of a bacterial enterotoxin potentially derived from a mammalian adamalysin/ADAM xenolog. *Proc Natl Acad Sci U S A.* 2011;108:1856–1861.
- Kling JJ, Wright RL, Moncrief JS, Wilkins TD. Cloning and characterization of the gene for the metalloprotease enterotoxin. *FEMS Microbiol Lett.* 1997;146:279–284.
- Franco AA. The *Bacteroides fragilis* pathogenicity Island is contained in a putative novel conjugative transposon. *J Bacteriol.* 2004;186:6077–6092.
- Buckwold SL, Shoemaker NB, Sears CL, Franco AA. Identification and characterization of conjugative transposons CTn86 and CTn9343 in *Bacteroides fragilis* strains. *Appl Environ Microbiol.* 2007;73:53–63.
- Wu S, Lim KC, Huang J, Saidi RF, Sears CL. *Bacteroides fragilis* enterotoxin cleaves the *zonula adherens* protein, E-cadherin. *Proc Natl Acad Sci USA.* 1998;95:14979–14984.
- Wu S, Rhee KJ, Zhang M, Franco A, Sears CL. *Bacteroides fragilis* toxin stimulates intestinal epithelial cell shedding and γ -secretase-dependent E-cadherin cleavage. *J Cell Sci.* 2007;120:1944–1952.
- Wong SH, Yu J. Gut microbiota in colorectal cancer: Mechanisms of action and clinical applications. *Nat Rev Gastroenterol Hepatol.* 2019;16:690–704.
- Purcell RV, Pearson J, Aitchison A, Dixon L, Frizelle FA, Keenan JI. Colonization with enterotoxigenic *Bacteroides fragilis* is associated with early-stage colorectal neoplasia. *PLoS One.* 2017;12:1–10.
- Rhee K-J, Wu S, Wu X, et al. Induction of persistent colitis by a human commensal, enterotoxigenic *Bacteroides fragilis*, in wild-type C57BL/6 mice. *Infect Immun.* 2009;77:1708–1718.
- Sanfilippo L, Li CK, Seth R, Balwin TJ, Menozzi MG, Mahida YR. *Bacteroides fragilis* enterotoxin induces the expression of IL-8 and transforming growth factor-beta (TGF- β) by human colonic epithelial cells. *Clin Exp Immunol.* 2000;119:456–463.
- Kim JM, Cho SJ, Oh YK, Jung HY, Kim YJ, Kim N. Nuclear factor-kappa B activation pathway in intestinal epithelial cells is a major regulator of chemokine gene expression and neutrophil migration induced by *Bacteroides fragilis* enterotoxin. *Clin Exp Immunol.* 2002;130:59–66.
- Wu S, Morin PJ, Maouyo D, Sears CL. *Bacteroides fragilis* enterotoxin induces c-Myc expression and cellular proliferation. *Gastroenterology.* 2003;124:392–400.
- Cuchural CJ, Tally FP. *Bacteroides fragilis*: Current susceptibilities, mechanisms of drug resistance, and principles of antimicrobial therapy. *Drug Intell Clin Pharm.* 1986;20:567–573.
- Shah N, Osmon D, Tande AJ, et al. Clinical and microbiological characteristics of *Bacteroides* prosthetic joint infections. *J Bone Jt Infect.* 2017;2:122–126.
- Treviño M, Areses P, Peñalver MD, et al. Susceptibility trends of *Bacteroides fragilis* group and characterisation of carbapenemase-producing strains by automated REP-PCR and MALDI TOF. *Anaerobe.* 2012;18:37–43.
- Aldridge KE, Ashcraft D, Cambre K, Pierson CL, Jenkins SG, Rosenblatt JE. Multicenter survey of the changing in vitro antimicrobial susceptibilities of clinical isolates of *Bacteroides fragilis* group, *Prevotella*, *Fusobacterium*, *Porphyromonas*, and *Peptostreptococcus* species. *Antimicrob Agents Chemother.* 2001;45:1238–1243.
- Betriu C, Culebras E, Gómez M, López F, Rodríguez-Avial I, Picazo JJ. Resistance trends of the *Bacteroides fragilis* group over a 10-year period, 1997 to 2006, in Madrid, Spain. *Antimicrob Agents Chemother.* 2008;52:2686–2690.
- Abian O, Vega S, Sancho J, Velazquez-Campoy A. Allosteric inhibitors of the NS3 protease from the hepatitis C virus. *PLoS One.* 2013;8:1–10.
- Hawe A, Sutter M, Jiskoot W. Extrinsic fluorescent dyes as tools for protein characterization. *Pharm Res.* 2008;25:1487–1499.
- Arolas JL, Goulas T, Cuppari A, Gomis-Rüth FX. Multiple architectures and mechanisms of latency in metallopeptidase zymogens. *Chem Rev.* 2018;118:5581–5597.
- Liebschner D, Afonine PV, Moriarty NW, et al. Polder maps: Improving OMIT maps by excluding bulk solvent. *Acta Crystallogr D Struct Biol.* 2017;73(Pt 2):148–157.
- Adams PD, Afonine PV, Bunkóczi G, et al. PHENIX: A comprehensive python-based system for macromolecular structure solution. *Acta Crystallogr Sect D Biol Crystallogr.* 2010;66:213–221.
- Emsley P, Cowtan K. Coot: Model-building tools for molecular graphics. *Acta Crystallogr D Biol Crystallogr.* 2004;60:2126–2132.
- Krissinel E, Henrick K. Inference of macromolecular assemblies from crystalline state. *J Mol Biol.* 2007;372:774–797.
- De Francesco R, Urbani A, Nardi MC, Tomei L, Steinkühler C, Tramontano A. A zinc binding site in viral serine proteinases. *Biochemistry.* 1996;35:13282–13287.
- Wright DL, Holloway JH, Reilley CN. Heats and entropies of formation of metal chelates of polyamine and polyaminocarboxylate ligands. *Anal Chem.* 1965;37:884–892.

35. Sillen LG, Martell AE, Bjerrum J. Stability constants of metal-ion complexes. London: Chemical Society, 1964.
36. Abian O, Vega S, Neira JL, Velazquez-Campoy A. Conformational stability of hepatitis C virus NS3 protease. *Biophys J*. 2010;99:3811–3820.
37. Colvin RA, Holmes WR, Fontaine CP, Maret W. Cytosolic zinc buffering and muffling: Their role in intracellular zinc homeostasis. *Metallomics*. 2010;2:306–317.
38. Outten CE, O'Halloran TV. Femtomolar sensitivity of metalloregulatory proteins controlling zinc homeostasis. *Science*. 2001;292:2488–2492.
39. Sensi SL, Paoletti P, Bush AI, Sekler I. Zinc in the physiology and pathology of the CNS. *Nat Rev Neurosci*. 2009;10:780–791.
40. Hara T, Takeda TA, Takagishi T, Fukue K, Kambe T, Fukada T. Physiological roles of zinc transporters: Molecular and genetic importance in zinc homeostasis. *J Physiol Sci*. 2017;67:283–301.
41. Tsai CJ, Nussinov R. A unified view of 'how allostery works'. *PLoS Comput Biol*. 2014;10:e1003394.
42. Wyman J, Gill SJ. Binding and linkage: Functional chemistry of biological macromolecules. Mill Valley: University Science Books, 1990.
43. Velazquez-Campoy A, Sancho J, Abian O, Vega S. Biophysical screening for identifying pharmacological chaperones and inhibitors against conformational and infectious diseases. *Curr Drug Targets*. 2016;17:1492–1505.
44. Goulas T, Cuppari A, Garcia-Castellanos R, et al. The pCri system: A vector collection for recombinant protein expression and purification. *PLoS One*. 2014;9:e112643.
45. Pantoliano MW, Petrella EC, Kwasnoski JD, et al. High-density miniaturized thermal shift assays as a general strategy for drug discovery. *J Biomol Screen*. 2001;6:429–440.
46. Matulis D, Kranz JK, Salemme FR, Todd MJ. Thermodynamic stability of carbonic anhydrase: Measurements of binding affinity and stoichiometry using thermofluor. *Biochemistry*. 2005;44:5258–5266.
47. Lo M-C, Aulabaugh A, Jin G, et al. Evaluation of fluorescence-based thermal shift assays for hit identification in drug discovery. *Anal Biochem*. 2004;332:153–159.
48. Cremades N, Velazquez-Campoy A, Martinez-Julvez M, et al. Discovery of specific flavodoxin inhibitors as potential therapeutic agents against *Helicobacter pylori* infection. *ACS Chem Biol*. 2009;4:928–938.
49. Neira JL, Bintz J, Arruebo M, et al. Identification of a drug targeting an intrinsically disordered protein involved in pancreatic adenocarcinoma. *Sci Rep*. 2017;7:39732.
50. Pey AL, Ying M, Cremades N, et al. Identification of pharmacological chaperones as potential therapeutic agents to treat phenylketonuria. *J Clin Invest*. 2008;118:2858–2867.
51. Paketurytė V, Petrauskas V, Zubrienė A, et al. Uncertainty in protein–ligand binding constants: Asymmetric confidence intervals versus standard errors. *Eur Biophys J*. 2021;50:661–670.
52. Kabsch W. XDS. *Acta Crystallogr sect D Biol Crystallogr*. 2010;66:125–132.
53. Kabsch W. Integration, scaling, space-group assignment and post-refinement. *Acta Crystallogr Sect D Biol Crystallogr*. 2010;66:133–144.
54. Blanc E, Roversi P, Vonnrhein C, Flensburg C, Lea SM, Bricogne G. Refinement of severely incomplete structures with maximum likelihood in BUSTER-TNT. *Acta Crystallogr Sect D Biol Crystallogr*. 2004;60:2210–2221.
55. Winn MD, Ballard CC, Cowtan KD, et al. Overview of the CCP4 suite and current developments. *Acta Crystallogr Sect D Biol Crystallogr*. 2011;67:235–242.
56. McCoy AJ, Grosse-Kunstleve RW, Adams PD, Winn MD, Storoni LC, Read RJ. Phaser crystallographic software. *J Appl Cryst*. 2007;40:658–674.
57. Salentin S, Schreiber S, Haupt VJ, Adasme MF, Schroeder M. PLIP: Fully automated protein–ligand interaction profiler. *Nucleic Acids Res*. 2015;43:443–447.
58. Adasme MF, Linnemann KL, Bolz SN, et al. PLIP 2021: Expanding the scope of the protein–ligand interaction profiler to DNA and RNA. *Nucleic Acids Res*. 2021;49:530–534.
59. DeLano WL. The case for open-source software in drug discovery. *Drug Discov Today*. 2005;10:213–217.

SUPPORTING INFORMATION

Additional supporting information can be found online in the Supporting Information section at the end of this article.

How to cite this article: Jimenez-Alesanco A, Eckhard U, Asencio del Rio M, Vega S, Guevara T, Velazquez-Campoy A, et al. Repositioning small molecule drugs as allosteric inhibitors of the BFT-3 toxin from enterotoxigenic *Bacteroides fragilis*. *Protein Science*. 2022;31(10):e4427. <https://doi.org/10.1002/pro.4427>